Journal of Glaciology

Article

Cite this article: Man M, Yang K, Chen D, Zhu Y, Wang Y (2025) Estimating supraglacial lake depth in Greenland: A comparison study of empirical formula, radiative transfer and depression topography methods. *Journal of Glaciology* **71**, e41, 1–15. https://doi.org/10.1017/jog.2025.23

Received: 12 June 2024
Revised: 28 February 2025
Accepted: 11 March 2025

Keywords:
ArcticDEM; Greenland Ice Sheet; ICESat-2; lake depth estimation; supraglacial lake

Corresponding author: Kang Yang;
Email: yangkangnju@gmail.com

cambridge.org/jog

Estimating supraglacial lake depth in Greenland: A comparison study of empirical formula, radiative transfer and depression topography methods

Mengtian Man[1], Kang Yang[1,2,3], Dinghua Chen[1], Yuxin Zhu[1] and Yuhan Wang[1]

[1]School of Geography and Ocean Science, Nanjing University, Nanjing, China; [2]Jiangsu Provincial Key Laboratory of Geographic Information Science and Technology, Nanjing, China and [3]Southern Marine Science and Engineering Guangdong Laboratory, Zhuhai, China

Abstract

Numerous supraglacial lakes form on the Greenland Ice Sheet (GrIS) during the summer, and accurately estimating their depth is crucial for understanding GrIS water storage. In this study, we estimate the depth of 35 representative GrIS supraglacial lakes using ICESat-2, Sentinel-2 imagery and ArcticDEM data. ICESat-2-derived lake depth is used to validate the performance of three remote sensing methods, namely empirical formula method (EFM), radiative transfer method (RTM) and depression topography method (DTM). EFM relies on ICESat-2-derived lake depth to construct empirical formulas, while RTM and DTM do not. The results show that (1) the green band EFM performs best; the DTM performs secondarily but tends to consistently underestimate depths; the green-band RTM has lower accuracy and overestimates depths, while the red-band RTM also has lower accuracy but underestimates depths. (2) Temporal changes of depression topography have limited impacts on the performance of DTM, whereas the uncertainties caused by lake shoreline height estimates should be considered. (3) The performance of RTM is significantly influenced by the spectral attenuation coefficient. We further identify the factors that affect spatiotemporal extrapolation of these methods and recommend prioritizing the use of the EFM when near-simultaneous ICESat-2 data are available; otherwise, DTM is recommended, yet an underestimation ratio should be used.

1. Introduction

Each summer, surface meltwater flows into topographic depressions and forms numerous supraglacial lakes on the Greenland Ice Sheet (GrIS) (Sundal and others, 2009; Banwell and others, 2014; Dunmire and others, 2021; Zhang and others, 2023). Some of these supraglacial lakes may undergo hydrofracturing at their bottoms and drain large volumes of meltwater through the ice sheet to the bed, consequently affecting ice sheet motion and stability (Das and others, 2008; Williamson and others, 2018b; Tuckett and others, 2019). Therefore, accurately estimating the supraglacial lake depth is crucial for analyzing surface meltwater storage on the GrIS and consequently improving our understanding of the GrIS mass balance.

Until now, only a few field measurements of GrIS supraglacial lake depth have been reported. For example, Box and Ski (2007) measured the depth of two supraglacial lakes (1.05–11.5 m and 1.25–10.0 m) on the western GrIS using a raft equipped with a depth sounder. Tedesco and Steiner (2011) measured the depth of the Olivia supraglacial lake (max depth 4.6 m) on the western GrIS using remote-controlled boats equipped with GPS and sonar. Legleiter and others (2014) measured the depth of the Napoli supraglacial lake (max depth 10.5 m) on the southwestern GrIS using remote-controlled boats equipped with GPS and sonar. Fitzpatrick and others (2014) measured the depth of two supraglacial lakes on the southwestern GrIS (max depth $\sim$ 12 and 16 m) using a raft equipped with GPS and a depth sounder. More recently, Lutz and others (2024) measured the depth of four supraglacial lakes (max depth $\sim$ 14 m) in the northeastern GrIS using a self-built remote-controlled boat equipped with a sonar sensor. However, the spatiotemporal coverage of these field measurements has been limited, mainly owing to the harsh GrIS natural conditions.

In recent years, the Ice, Clouds, and Land Elevation Satellite-2 (ICESat-2) raises new prospects for estimating supraglacial lake depth. The ICESat-2 photon clouds can penetrate water and thereby capture the surface and bottom elevation of shallow water simultaneously with high precision (Ranndal and others, 2021; Xu and others, 2021; Bernardis and others, 2023). Previous studies distinguished the photon clouds of the supraglacial lake surface and bottom using kernel density estimation algorithms and then estimated the lake depth accordingly

(Fair and others, 2020; Datta and Wouters, 2021; Xiao and others, 2023). However, one ICESat-2 photon track can only generate one corresponding depth profile; it cannot generate complete lake bathymetry. Therefore, in supraglacial lake studies (and more broadly, in nearshore shallow water studies), ICESat-2-derived water depths are commonly used for accuracy validation or are combined with passive optical satellite imagery to generate complete water bathymetry (Albright and Glennie, 2020; Ma and others, 2020; Datta and Wouters, 2021; Hsu and others, 2021).

Currently, there are three remote sensing methods commonly used for estimating supraglacial lake depth (Table 1), namely the empirical formula method (EFM), radiative transfer method (RTM), and depression topography method (DTM). The EFM combines field or ICESat-2-derived lake depth measurements with the corresponding single- or dual-band reflectance of passive optical satellite imagery (e.g. Sentinel-2, Landsat-8, and Planet) to construct empirical regression formulas, and the obtained formula is then applied to calculate lake bathymetry (Legleiter and others, 2014; Pope and others, 2016; Datta and Wouters, 2021). The RTM builds on the physical principle that the radiation of incident light decreases as depth increases (Lyzenga, 1978; Philpot, 1989) and combines optical image bands (e.g. MODIS, Sentinel-2, and Landsat-8) with pre-defined coefficients (e.g. scattering attenuation coefficients of upward and downward light) to estimate depth variation (Ignéczi and others, 2016; Pope and others, 2016; Melling and others, 2024). The DTM generates ice surface depressions using the pre- or post-melt season digital elevation models (DEMs, e.g. WorldView-2 DEM, ArcticDEM and TanDEM-X) and intersects the depression topography with the satellite-mapped lake shorelines to estimate lake bathymetry (Moussavi and others, 2016; Yang and others, 2019; Lutz and others, 2024; Melling and others, 2024).

Until recently, these three methods have been widely used, so it is crucial for comparing their performances. Pope and others (2016) used the field-measured lake depth (max depth 5 m) on the southwestern GrIS to compare the performance of the RTM and the dual-band EFM. Moussavi and others (2016) used DTM to estimate the depth of 14 supraglacial lakes (max depth 7 m) on the southwestern GrIS, and the resultant depth was employed as validation data to compare with RTM and EFM. Melling and others (2024) compared the performance of ICESat-2, RTM, and DTM to estimate the depths of five supraglacial lakes (max depth 3.2–7.9 m) on the southwestern GrIS. Lutz and others (2024) used DTM to estimate the depth of 5 supraglacial lakes (max depth $\sim$ 27.6 m) on the northeastern GrIS, providing validation data for comparison with RTM, ICESat-2-EFM and Sonar-EFM. Most recently, Zhou and others (2025) used ICESat-2-derived depths from seven supraglacial lakes (max depth $\sim$ 3.4–8.5 m) as validation to compare the performance of RTM, EFM, and two machine learning algorithms. Although these comparisons provide valuable information to guide depth estimation method selection, we suggest that a more detailed comparison should be conducted. First, the ICESat-2-derived depth data can be used as validation data, whereas DTM should be employed as a comparative method rather than validation data (Moussavi and others, 2016; Pope and others, 2016; Yang and others, 2019). Second, EFM, RTM, and DTM should all be involved in comparisons. Third, the depth ranges and numbers of the supraglacial lakes selected in most previous studies are limited, and more representative supraglacial lakes (particularly deep lakes, which may most challenge estimation methods) on the entire GrIS should be used. For these purposes, in this study, we select 35 supraglacial lakes with a large depth variation (max depth 2.3–12.3 m) from various regions of GrIS and use the ICESat-2-derived supraglacial lake depth as validation data to compare the performance of EFM, RTM, and DTM.

2. Data and study lakes

2.1. Data

ICESat-2 is equipped with the Advanced Topographic Laser Altimeter System (ATLAS), which utilizes green (wavelength 532 nm) laser light and single-photon sensitive detection to measure surface height along each of its six beams (Markus and others, 2017). ICESat-2 produces footprints on the ground spaced $\sim$0.7 m along the track and is capable of penetrating water up to $\sim$40 m (Parrish and others, 2019; Ranndal and others, 2021). ICESat-2 ATL03 is a global geolocated photon data product with a measurement accuracy of 5 cm and a precision of 13 cm (Brunt and others, 2019), and this product can capture both surface and bottom photon clouds of lakes (Jasinski and others, 2023). ICESat-2 ATL06 is a land ice elevation product produced by fitting the ATL03 photon data as a function of along-track distance with a linear model in each 40 m segment (Smith and others, 2019), with a measurement accuracy of 3 cm and a precision of 9 cm (Brunt and others, 2019). In this study, we use the ICESat-2 ATL06 data to determine the photon cloud scope of the ICESat-2 ATL03 and to remove a portion of noise photons, and the ICESat-2 ATL03 data to measure the depth of supraglacial lakes.

Sentinel-2A/B are earth observation satellites launched by European Space Agency Copernicus program, with a 290 km swath width and a revisit period of less than 5 days. The Sentinel-2A/B images cover 13 spectral bands, including visible, near-infrared (NIR), and shortwave infrared, with a 10 m spatial resolution for visible and NIR bands (Drusch and others, 2012). In this study, we use the Sentinel-2 Level-2A surface reflectance product to identify the extent of a supraglacial lake and to build EFM and RTM depth estimation formulas. All images are acquired through the Google Earth Engine (GEE) platform (https://earthengine.google.com/).

ArcticDEM, released by the Polar Geospatial Center, is a high-resolution digital surface model for the entire Arctic region. ArcticDEM is generated from WorldView-1/2/3 and GeoEye-1 optical stereo imagery using Surface Extraction software with TIN-based Search-Space Minimization, which has the validation accuracy of 0.2 m (Noh and Howat, 2015). In this study, we use the 2 m-resolution ArcticDEM strip data (version s2s041) (Porter and others, 2022) to derive ice surface depression topography. Importantly, the ArcticDEM data used in this study are made by using pre- or post-melt season optical stereo imagery, ensuring that the studied ice surface depressions are not covered by supraglacial lakes, following Moussavi and others (2016), Yang and others (2019), and Melling and others (2024).

2.2. Study lakes

We select 35 supraglacial lakes across various regions of the GrIS (Fig. 1), based on the following criteria: first, near-simultaneous ($\pm$3 days) ICESat-2 tracks and Sentinel-2 imagery are available. Second, ICESat-2 tracks do not cross floating ice on the supraglacial lake. Third, ArcticDEM data from the same year during the dry period (determined by visually inspecting near-simultaneous Sentinel-1/2 imagery in GEE) of the selected lake is available. The selected lakes cover a maximum depth range of 2.3 to 12.3 m, providing continuous depth observations (at least one lake per meter of depth range).

Table 1. Summary of supraglacial lake depth estimation studies, including field measurements, ICESat-2-derived algorithms, empirical formula method (EFM), radiative transfer method (RTM), and depression topography method (DTM)

Method	Source	Data source
Field measurements	Box and Ski (2007)	GPS, sonar
	Tedesco and Steiner (2011)	GPS, sonar
	Legleiter and others (2014)	GPS, sonar
	Fitzpatrick and others (2014)	GPS, sonar
	Lutz and others (2024)	GPS, sonar
ICESat-2	Neuenschwander and Pitts (2019)	ATL03
	Jasinski and others (2023)	ATL03
	Fair and others (2020)	ATL03, ATL06
	Fricker and others (2021)	ATL03
	Datta and Wouters (2021)	ATL03, ATL06
	Xiao and others (2023)	ATL03
	Arndt and Fricker (2024)	ATL03
Empirical formula method (EFM)	Box and Ski (2007)	MODIS (red band)
	Fitzpatrick and others (2014)	MODIS (red band)
	Legleiter and others (2014)	Landsat-7, MOSID, ASTER, WorldView-2 (visible and near-infrared bands)
	Moussavi and others (2016)	Landsat-7, WorldView-2 (visible, red edge, and near-infrared bands)
	Pope and others (2016)	Landsat-7, Landsat-8 (coastal, blue, green, red, and panchromatic bands)
	Williamson and others (2018a)	Sentinel-2 (red, green, and blue bands)
	Datta and Wouters (2021)	Landsat-8, Sentinel-2, SkySat, Planet (red and green bands)
	Lutz and others (2024)	Sentinel-2 (blue, green, and red bands)
	Fan and others (2025)	Landsat-7, Landsat-8 (coastal, blue, green, NIR, and panchromatic bands)
	Zhou and others (2025)	Landsat-8, Sentinel-2 (coastal, blue, and green bands)
Radiative transfer method (RTM)	Sneed and Hamilton (2007)	ASTER (green band)
	Georgiou and others (2009)	ASTER (green band)
	Sneed and Hamilton (2011)	ASTER, Landsat-7 (green band)
	Morriss and others (2013)	Landsat-7, MODIS (red band)
	Johansson and Brown (2013)	MODIS (green band)
	Banwell and others (2014)	Landsat-7 (green band)
	Langley and others (2016)	Landsat-7, ASTER (red band)
	Ignéczi and others (2016)	MODIS (red band)
	Moussavi and others (2016)	Landsat-7, WorldView-2 (red, green, and blue bands)
	Pope and others (2016)	Landsat-7, Landsat-8 (red and panchromatic bands)
	Williamson and others (2017)	MODIS, Landsat-8 (red and green bands)
	Moussavi and others (2020)	Landsat-8 (red and panchromatic bands)
	Arthur and others (2020)	Sentinel-2, Landsat-7, Landsat-8 (red and panchromatic bands)
	Zhu and others (2022)	Landsat-8 (red and panchromatic bands)
	Melling and others (2024)	Sentinel-2 (red and green bands)
	Lutz and others (2024)	Sentinel-2 (green band)
	Rowley and others (2024)	Landsat-8 (red and panchromatic bands)
	Fan and others (2025)	Landsat-7, Landsat-8 (red and panchromatic bands)
	Zhou and others (2025)	Landsat-8, Sentinel-2 (red and green bands)
Depression topography method (DTM)	Moussavi and others (2016)	WorldView-2 DEM
	Pope and others (2016)	WorldView-2 DEM
	Yang and others (2019)	ArcticDEM
	Melling and others (2024)	ArcticDEM
	Lutz and others (2024)	TanDEM-X
	Rowley and others (2024)	ArcticDEM

These 35 lakes are ranked as Lakes 1–35 in terms of their maximum depth. Lakes 1–12 are classified as shallow lakes (max depth 2.3–4.8 m), while Lakes 13–35 are classified as deep lakes (max depth 5.4–12.3 m), based on a 5 m threshold for maximum lake depth. This 5 m threshold represents the maximum penetration depth of the red band and is widely used in previous supraglacial lake studies (Moussavi and others, 2016; Pope and others, 2016; Melling and others, 2024). Therefore, we followed this depth threshold to make our results comparable with previous studies. The data used for depth estimation are listed in Table S1.

3. Methods

3.1. ICESat-2 Watta lake depth estimation method

We use the Watta algorithm (Datta and Wouters, 2021) to derive supraglacial lake depth profiles from ICESat-2 at the native 0.7 m resolution of ATL03 photon clouds. First, this algorithm selects the ATL03 photon clouds within a distance of 50 m around the elevation of the corresponding ICESat-2 ATL06 photons to remove a portion of noise photons. Second, a sliding window of 75 ATL03 photons is applied to generate a probability density curve of photon elevations within each window through kernel density estimation. The two obtained elevation values with the highest probability density within each window are assigned as the lake surface and bottom elevations, respectively. Third, to obtain more reliable lake bottom elevations, the Watta algorithm conducts kernel density estimation again in a larger window of 5,000 ATL03 photons to remove the outliers of the bottom elevations due to the low photon density there. Fourth, the depth of each photon point is calculated by subtracting the lake bottom elevation from the lake surface elevation and applying a refractive index of ~0.75 to remove the refraction influence:

$$\text{Lake depth} = (\text{Lake surface elevation} - \text{Lake bottom elevation}) * 0.75 \quad (1)$$

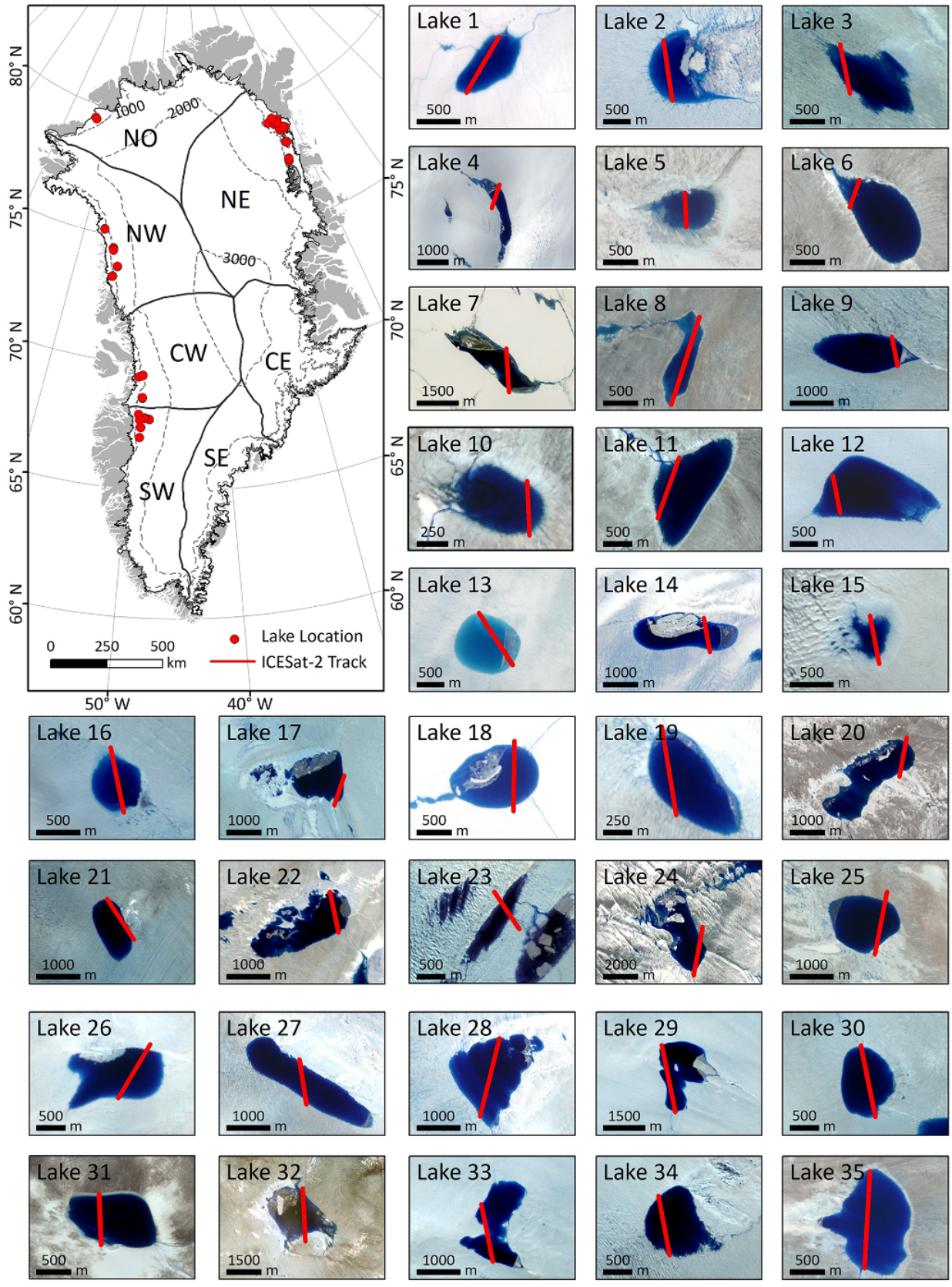

Figure 1. Thirty-five study supraglacial lakes on the Greenland ice sheet are used to compare three remote sensing depth estimation methods. Sentinel-2 images (R: NIR band, G: red band, B: green band) of these lakes are depicted in the subplots, with the red lines indicating the ICESat-2 track. The subplot in the left corner shows the locations of these supraglacial lakes on the gris marked with red dots.

The corrected lake bottom elevation is then derived as:

$$\text{Lake bottom elevation after refraction correction} = \text{Lake surface elevation} - \text{Lake depth} \quad (2)$$

In this study, we use Sentinel-2 green and NIR bands to calculate the Normalized Difference Water Index ($NDWI = (green - NIR)/(green + NIR)$, *green* and *NIR* are the reflectance of green and NIR bands, respectively) (McFeeters, 1996), with a threshold of 0.3 to extract water masks and generate supraglacial lake shorelines. The ICESat-2 ATL03 photon points within each lake shoreline are then extracted and stratified at 1 m intervals of lake depth to avoid uneven distribution of water depths at sample points due to random sampling. Next, 70% of the photon points from each meter depth are randomly selected to form the training dataset, with the remaining 30% points used as validation data, ensuring a balanced evaluation of model training and validation (Nguyen and others, 2021).

3.2. EFM

The EFM attempts to establish exponential, quadratic, or logarithmic empirical regression formulas between field-measured or ICESat-2-derived lake depth and the corresponding pixel reflectance of optical remote sensing imagery (Box and Ski, 2007; Williamson and others, 2018a). The quadratic formula, widely used in previous studies (Legleiter and others, 2014; Moussavi and others, 2016; Pope and others, 2016), is selected in this study for comparison. We build the quadratic empirical formula by fitting the Sentinel-2 water pixel reflectance and ICESat-2-derived supraglacial lake depth following Datta and Wouters (2021):

$$Z = a + bX + cX^2 \quad (3)$$

$$X = \ln\left(\frac{R_1}{R_2}\right) \quad (4)$$

where Z represents the estimated lake depth, a, b, and c are fitting parameters, and X represents the logarithm of the ratio of the reflectance of the two spectral bands, R_1 and R_2, in the Sentinel-2 imagery.

Moreover, we use the optimal band ratio analysis (OBRA) to select the optimal band combination following Legleiter and others (2009). First, a total number of $N(N-1)/2$ band combination ratios are obtained by pairing N bands. These band ratios are calculated, and then the training datasets are used to establish empirical formulas, with their R^2 and RMSE calculated. Next, the band combination with the highest R^2 and the lowest RMSE is determined as the optimal choice, and the associated depth estimates are then compared with other methods.

We conduct two experiments to analyze the spatiotemporal extrapolation of the EFM. Spatially, we construct an overall empirical formula based on all 35 study lakes, and then apply the resultant empirical formula to estimate lake depths for each lake. This experiment allows us to analyze the spatial stability of the overall empirical formula over space. Temporally, we select the supraglacial lakes covered by two different ICESat-2 tracks on different days. For each selected lake, we use the early-day ICESat-2 and Sentinel-2 imagery to construct the EFM, then apply the resultant empirical formula to estimate lake depths from the late-day Sentinel-2 imagery. Finally, we validate the estimated depths using the late-day ICESat-2-derived depths. This experiment allows us to analyze the temporal stability of the empirical formula over different depth ranges as the study lakes expand or shrink over time.

3.3. RTM

The RTM builds on the physical principle that incident radiation decreases with increasing water depth (Philpot, 1989), and assumes that the lake has few impurities, small particles, uniform lake bed sediment, and a relatively calm water surface with minimal wind and wave influence (Sneed and Hamilton, 2007). These assumptions are generally met in clean meltwater lakes, and therefore, the RTM has been widely used for estimating GrIS supraglacial lake depth before the advent of ICESat-2 (Sneed and Hamilton, 2007; Georgiou and others, 2009; Morriss and others, 2013; Langley and others, 2016). One key consideration of RTM is to select appropriate spectral bands, and numerous studies have shown that the shorter wavelengths allow for estimating deeper water depth due to their slower attenuation in the water (Moussavi and others, 2016; Pope and others, 2016). The green and red bands are most commonly used in previous studies (Table 1), and thereby, we also select these two bands. The RTM formulas are as follows:

$$Z = \frac{[ln\,(A_d - R_\infty) - ln\,(R_w - R_\infty)]}{g} \quad (5)$$

$$g \approx K_u + K_d \quad (6)$$

$$K_d = a + \frac{1}{2}b \quad (7)$$

where Z represents the lake depth, A_d is the lake bottom reflectance, R_∞ is the deep ocean reflectance, R_w is the lake pixel reflectance, g is the spectral attenuation coefficient, K_u and K_d represent the scattering attenuation coefficients of upward and downward light, respectively, a is the absorption coefficient for water, and b is the backscattering coefficient for water.

A_d is calculated as the average reflectance value in a 30 m-wide buffer around each lake shoreline following Moussavi and others (2020), and the standard deviation value is used to represent the uncertainty of A_d. We calculate the mean pixel reflectance in the deep ocean area of the imagery to estimate R_∞; and if no deep water is available in the imagery, the neighboring coastal imagery from the same period and orbit under similar atmospheric conditions is used, following Sneed and Hamilton (2007). Previous studies assumed that $K_d = K_u$ and thereby $g = 2K_d$ (Sneed and Hamilton, 2007; Banwell and others, 2014; Pope and others, 2016). In this study, we use $a_{green} = 0.0619\ m^{-1}$ and $a_{red} = 0.429\ m^{-1}$ (Pope and Fry, 1997), and $b_{green} = 0.0012\ m^{-1}$ and $b_{red} = 0.0006\ m^{-1}$ (Buiteveld and others, 1994) to calculate K_d, resulting in $g_{green} = 0.1250\ m^{-1}$ and $g_{red} = 0.8586\ m^{-1}$. For $g = mK_d$, although $m = 2$ is most commonly used, Kirk (1989) suggested that m should vary between 2 and 3.5 and Melling and others (2024) recommended $m = 2.75$. We conduct a sensitivity experiment to compare the estimated depths under different m values with a step size of 0.25.

3.4. DTM

The DTM estimates lake depth by intersecting the DEM-derived depression topography with the satellite-mapped lake shoreline (Moussavi and others, 2016; Pope and others, 2016; Yang and others, 2019). First, we fill the ArcticDEM data acquired during the dry period of a supraglacial lake, and subtract the data before and after filling to obtain the depression topography raster, with

each pixel value representing its elevation difference (i.e. height) from the depression outer boundary, following Karlstrom and Yang (2016). Next, we intersect the satellite-mapped lake shoreline with the depression topography to calculate the height of the lake shoreline. Ideally, the obtained shoreline height values should be equal; however, due to the accuracy limitation of the ArcticDEM data, the obtained height values vary considerably (Yang and others, 2019). Therefore, their average value is used to represent the lake shoreline height and their standard deviation to represent uncertainty. The average height value is subtracted from each depression topography pixel within the lake water mask to obtain the lake depth raster.

The ArcticDEM data and Sentinel-2 imagery we used are acquired at different dates, potentially impacting depth estimation due to changes in depression topography (Ignéczi and others, 2018). To mitigate this problem, we select ArcticDEM data obtained in the same year as the Sentinel-2 imagery to conduct method comparison. Moreover, to analyze the impact of ArcticDEM data selection on the lake depth estimation, we conduct a sensitivity experiment using multiple ArcticDEM data obtained ± 1 year from the Sentinel-2 imagery acquisition dates.

3.5. Indicators for validating accuracy

We validate the accuracy of the depths estimated by EFM, RTM, and DTM (D_{est}) with the ICESat-2-derived depth (D_{IS2}), using the following indicators: the coefficient of determination (R^2), bias, root mean square error (RMSE), and relative root mean squared error (RRMSE). The validation is formed using the 30% of the dataset, which is not involved in constructing the EFM. The evaluation metrics are calculated as follows:

$$R^2 = 1 - \frac{\sum (D_{est} - D_{IS2})^2}{\sum (D_{IS2} - \overline{D_{IS2}})^2} \tag{8}$$

$$Bias = \frac{1}{N} \sum (D_{est} - D_{IS2}) \tag{9}$$

$$RMSE = \sqrt{\left(\frac{\sum (D_{est} - D_{IS2})^2}{N} \right)} \tag{10}$$

$$RRMSE = \frac{RMSE}{\overline{D_{IS2}}} \tag{11}$$

where $\overline{D_{IS2}}$ is the mean of the ICESat-2-derived depths (D_{IS2}), and N is number of ICESat-2-derived depths used for the comparison.

For the DTM method specifically, we additionally calculate the underestimation ratio (UR) to quantify its tendency to underestimate lake depths. The UR is defined as:

$$UR = -\frac{1}{N} \sum \frac{(D_{DTM} - D_{IS2})}{D_{IS2}} \tag{12}$$

where D_{DTM} is the depth estimated by the DTM.

4. Results

4.1. Accuracy comparison of three methods

The ICESat-2-derived lake depth profiles are used to validate the performance of the three depth estimation methods, including the green-band EFM, green-band and red-band RTMs, and DTM (Figs. 2, 3, S1; Table S2). The results show that the green-band EFM is most accurate and stable, with an average of $R^2 = 0.93 \pm 0.06$, bias $= 0.00 \pm 0.03$ m, and RMSE $= 0.48 \pm 0.25$ m for the 35 lake profiles. The DTM yields the second-highest accuracy, with an average of $R^2 = 0.75 \pm 0.18$ and RMSE $= 0.95 \pm 0.45$ m, tending to underestimate lake depth (bias $= -0.60 \pm 0.55$ m). The green-band and red-band RTMs yield the lowest and most unstable accuracy, with an average of $R^2 = 0.60 \pm 0.09$ and 0.48 ± 0.11, and RMSE $= 2.79 \pm 1.10$ m and 2.74 ± 1.71 m, respectively. Additionally, the green-band RTM significantly overestimates lake depth (bias $= 2.62 \pm 1.13$ m), whereas the red-band RTM significantly underestimates (-2.01 ± 1.65 m) lake depth.

Shallow and deep lakes are analyzed separately to further compare the three depth estimation methods (Fig. 3; Table S2). The green-band EFM and DTM show no significant difference in estimating shallow and deep lake depths (Mann–Whitney U-test, $p > 0.05$), hence their performances are not sensitive to depth variations. However, the green-band RTM shows a significant difference (Mann–Whitney U-test, $p < 0.05$), performing well for deep lakes but substantially overestimating shallow lake depth ($R^2 = 0.66$ versus 0.42; bias $= 2.37$ m versus 3.41 m), while the red-band RTM also shows a significant difference (Mann–Whitney U-test, $p < 0.05$), performing well for shallow lakes but substantially underestimating deep lake depth ($R^2 = 0.63$ versus 0.41; bias $= -0.10$ m versus -3.00 m). This finding suggests that the performance of RTMs is very sensitive to lake depth variations.

4.2. Band optimization and spatiotemporal extrapolation of the EFM

OBRA is used to determine the optimal band combination for EFM, and the results show that the single green-band EFM performs best across all 35 lakes ($R^2 = 0.92 \pm 0.05$ and RMSE $= 0.48 \pm 0.25$ m) (Fig. 4). Dual blue-green bands, recommended by Moussavi and others (2016), perform very similarly to the single green band ($R^2 = 0.91 \pm 0.08$ and RMSE $= 0.54 \pm 0.37$ m) (Figs. 4a, b). In contrast, the red-band and dual red-other bands performs well for shallow lakes (Figs. 4c, d) but least accurate for deep lakes (Figs. 4e, f). This finding is consistent with previous results showing that the red-band EFM is only suitable for estimating shallow lake depth (max depth < 5 m), while the green-band and dual green-blue bands are suitable for deep lakes (max depth > 5 m) (Moussavi and others, 2016).

The reflectance-depth empirical formulas obtained from different lakes are considerably different (Fig. 5a; Table S2). Additionally, the overall empirical formula performs significantly poorer than the empirical formula constructed for each lake ($R^2 = 0.66 \pm 0.24$ versus 0.93 ± 0.06, RMSE $= 1.46 \pm 0.92$ versus 0.48 ± 0.25 m, bias $= 0.15 \pm 1.45$ versus 0.00 ± 0.03 m) (Fig. 5b). These findings indicate that the empirical formulas derived by the EFM vary considerably over space and its spatial extrapolation ability is limited.

Among our 35 lakes, there are six lakes covered by two different ICESat-2 tracks on different days (Fig. 6a). When validating with the independent late-day ICESat-2 tracks, the accuracy of the EFM decreases but remains higher than the RTM and the DTM (Figs. 6d–g). The EFM performs well within the depth range of the data used for construction, with estimated depths closely matching the ICESat-2-derived depths. In contrast, when extrapolated beyond this range, the estimated depths exhibit significant bias (Figs. 6b, c). This finding indicates that the EFM constructed for a specific lake captures some useful information about snow/ice

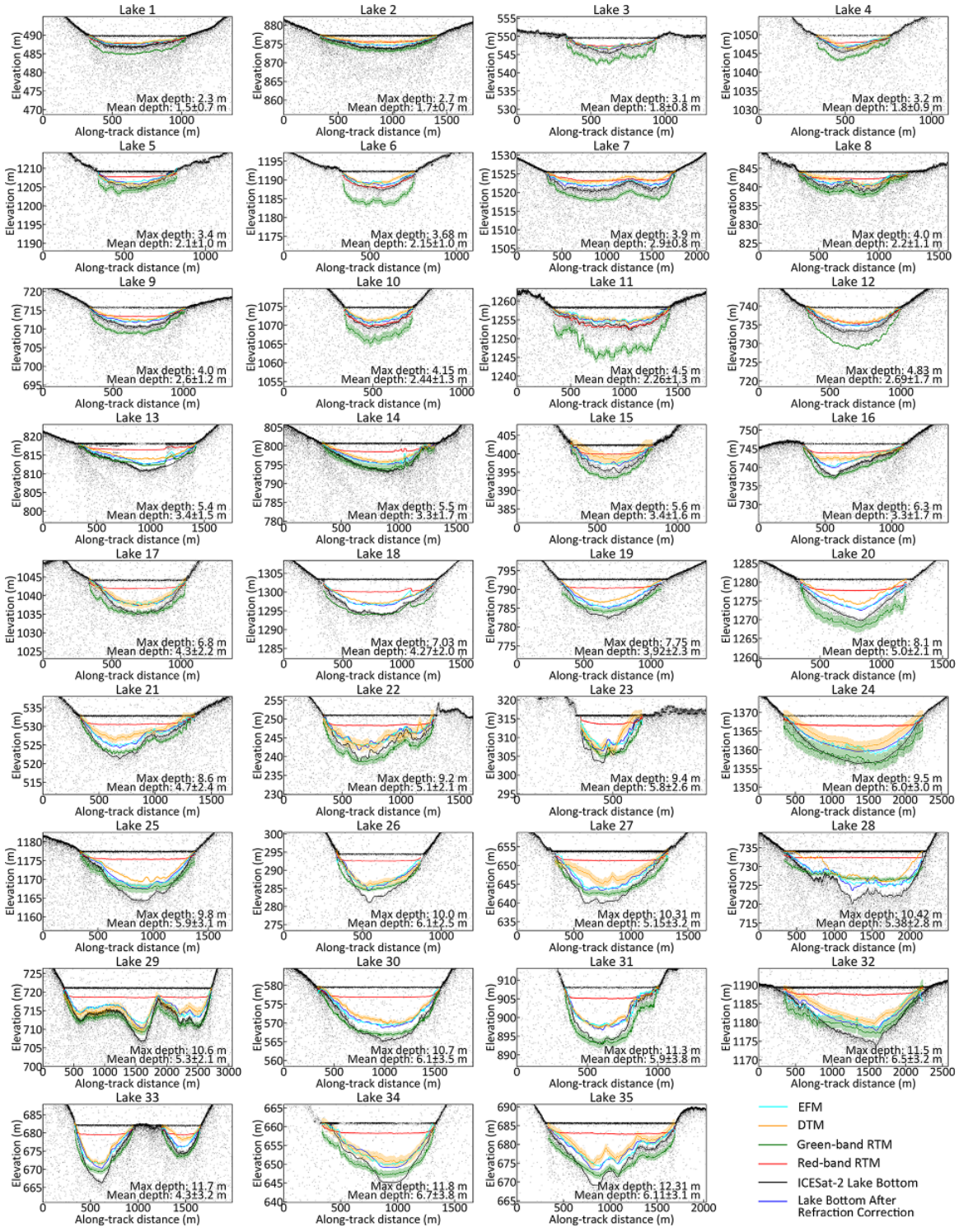

Figure 2. Depth profiles of 35 study supraglacial lakes estimated using various methods, with ICESat-2-derived lake bottoms in black and the lake bottom elevation after refraction correction in blue, depths estimated by the empirical formula method (EFM) in cyan, the green-band radiative transfer method (RTM) in green, the red-band RTM in red, and the depression topography method (DTM) in Orange. The range around each profile represents the uncertainty of the method.

surfaces beneath and near the lake (Fig. 6a), thereby allowing for the temporal extrapolation.

4.3. Sensitivity analysis of the attenuation coefficient in the RTM

The impacts of different spectral attenuation coefficient ($g = mK_d$) values on the performance of the RTM are evaluated (Fig. 7). The results show that the green-band RTM is more sensitive to m values than the red-band RTM, consistent with findings of Moussavi and others (2016) and Melling and others (2024). Additionally, the commonly used $m = 2$ for pure water induces the green-band RTM to significantly overestimate both shallow and deep lake depths, and induces the red-band RTM to significantly underestimate deep lake depth. Increasing m values can improve the green-band's performance for estimating both shallow and deep

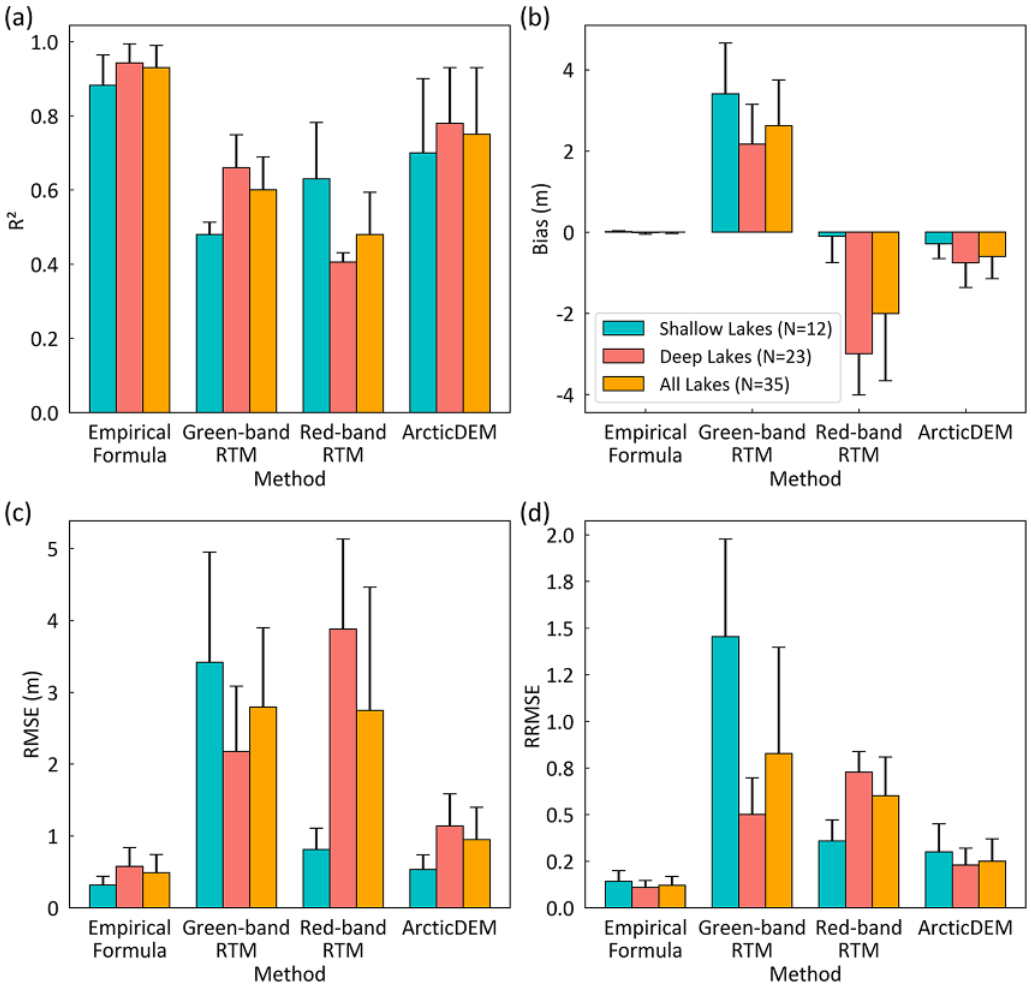

Figure 3. Comparison of the empirical formula method (EFM), the green-band and red-band radiative transfer method (RTM), and the depression topography method (DTM) with average (a) R^2, (b) bias, (c) RMSE, and (d) RRMSE (with the error bars showing the standard deviation) calculated for 12 shallow lakes (lakes 1–12, in green), 23 deep lakes (lakes 13–35, in red), and all 35 lakes (in Orange).

lake depth, with $m = 3$ minimizing the average bias for the green band RTM in deep (max depth $>$ 5 m) lakes (Fig. 7a). However, increasing m values declines red-band's performance for estimating both shallow and deep lake depth, with $m = 2$ minimizing the average bias for the red band RTM in shallow (max depth $<$ 5 m) lakes (Fig. 7b). Moreover, the A_d value calculated using the average reflectance of pixels around the lake shoreline also affects the depth estimates. Pixels around the lake shoreline with notable reflectance differences induce a large standard deviation of A_d value and consequently high depth uncertainty, as shown by the large depth range of Lake 20 and Lake 24 (Fig. 2).

4.4. Uncertainty analysis of the multi-period arcticdem DTM

Multi-period ArcticDEM data is used to analyze the impact of depression topography changes on the performance of the DTM (Fig. 8). Although the ArcticDEM-derived height variations (represented as standard deviations, ~0.2–1.6 m) of the lake shoreline pixels induce considerably large uncertainties in depth estimates of multi-period ArcticDEM DTMs (pale orange ranges in Fig. 2), their accuracy differences calculated from average height values of the lake shoreline pixels (orange lines in Fig. 2) remain smaller than their differences with other comparison methods (Fig. 2). For the 18 lakes with multi-period (2-5 times) strips of 2 m ArcticDEM data available (Fig. 8a), multi-period ArcticDEM DTMs are more accurate than the green-band and red-band RTMs, and particularly, for Lake 11 and 31, multi-period ArcticDEM DTM is even comparable to the best-performing green-band EFM (Figs. 8b, c). This finding suggests that the temporal changes of depression topography have limited impacts on the performance of the DTM, whereas the uncertainties caused by lake shoreline height estimates should be considered when conducting DTM.

5. Discussion

5.1. Applicability of the EFM

Our comparison shows that the EFM performs best in estimating supraglacial lake depth on the GrIS (Fig. 3; Table S2). This is predictable because it relies on synchronous ICESat-2 data to build empirical formulas, whereas RTM and DTM do not. However, the reflectance-depth empirical formulas obtained from different lakes are considerably different (Fig. 5a; Table S2), and the overall

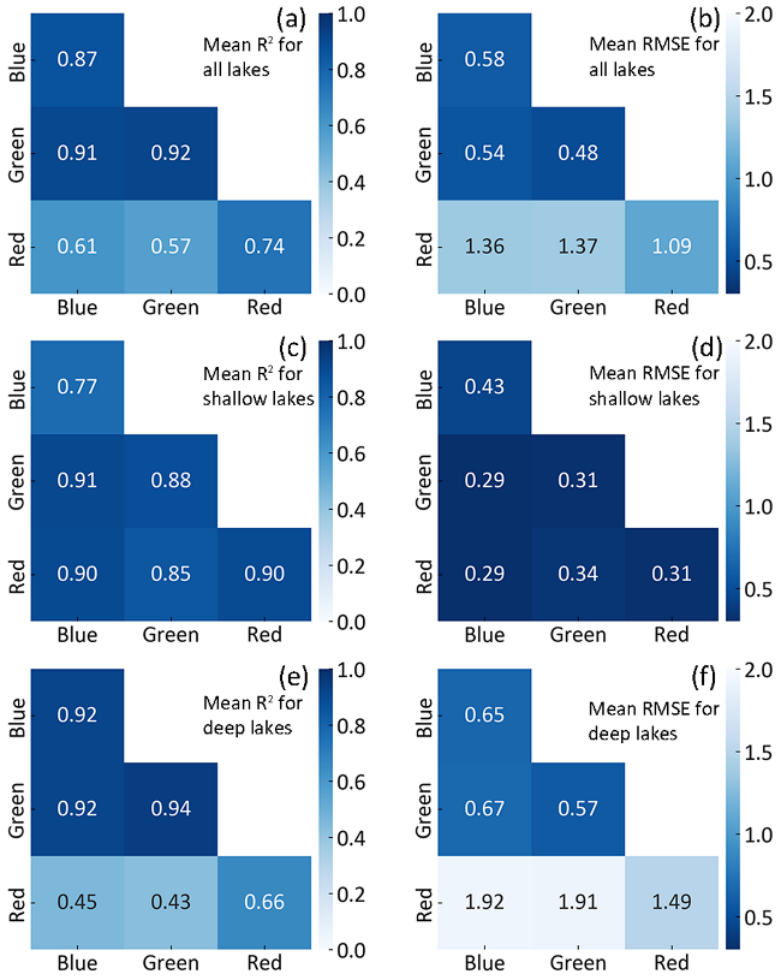

Figure 4. The R^2 and RMSE of the empirical formula method (EFM) calculated for each paired combination of blue, green, and red bands. (a) and (b) are for all 35 study supraglacial lakes, (c) and (d) for 12 shallow lakes, and (e) and (f) for 23 deep lakes.

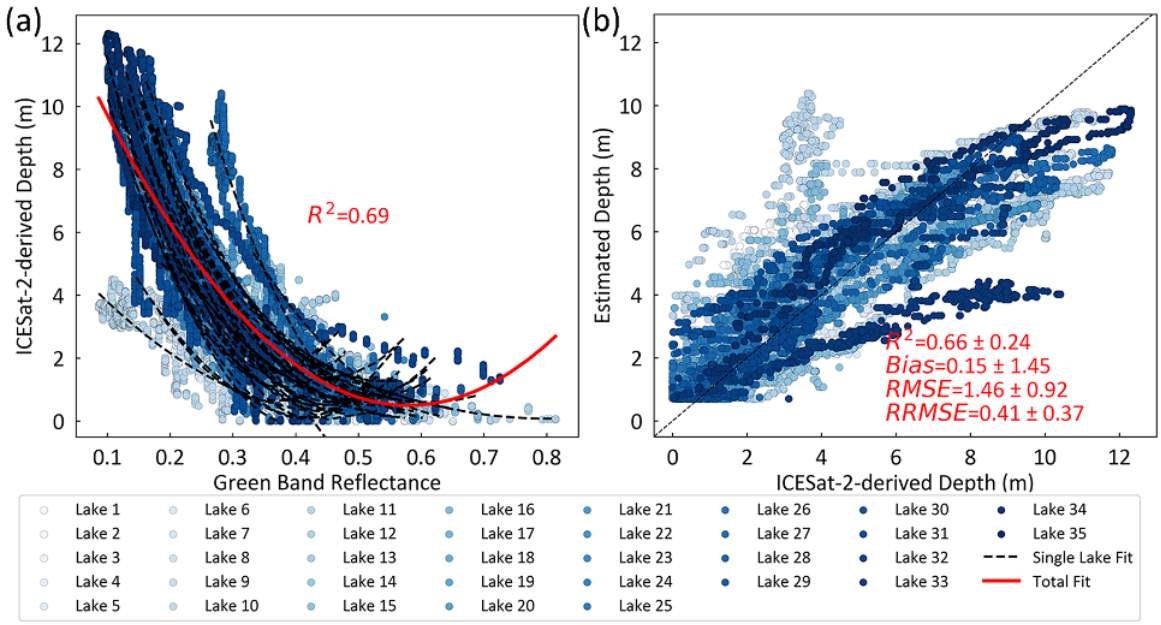

Figure 5. (a) Relationship between green band reflectance and ICESat-2-derived depth for the training data of 35 study lakes. The red solid line represents the overall fitted empirical formula, and the black dashed lines represent the 35 fitted empirical formulas. (b) Comparison of the overall EFM estimated lake depths and the ICESat-2-derived lake depths for the validation data of 35 study lakes.

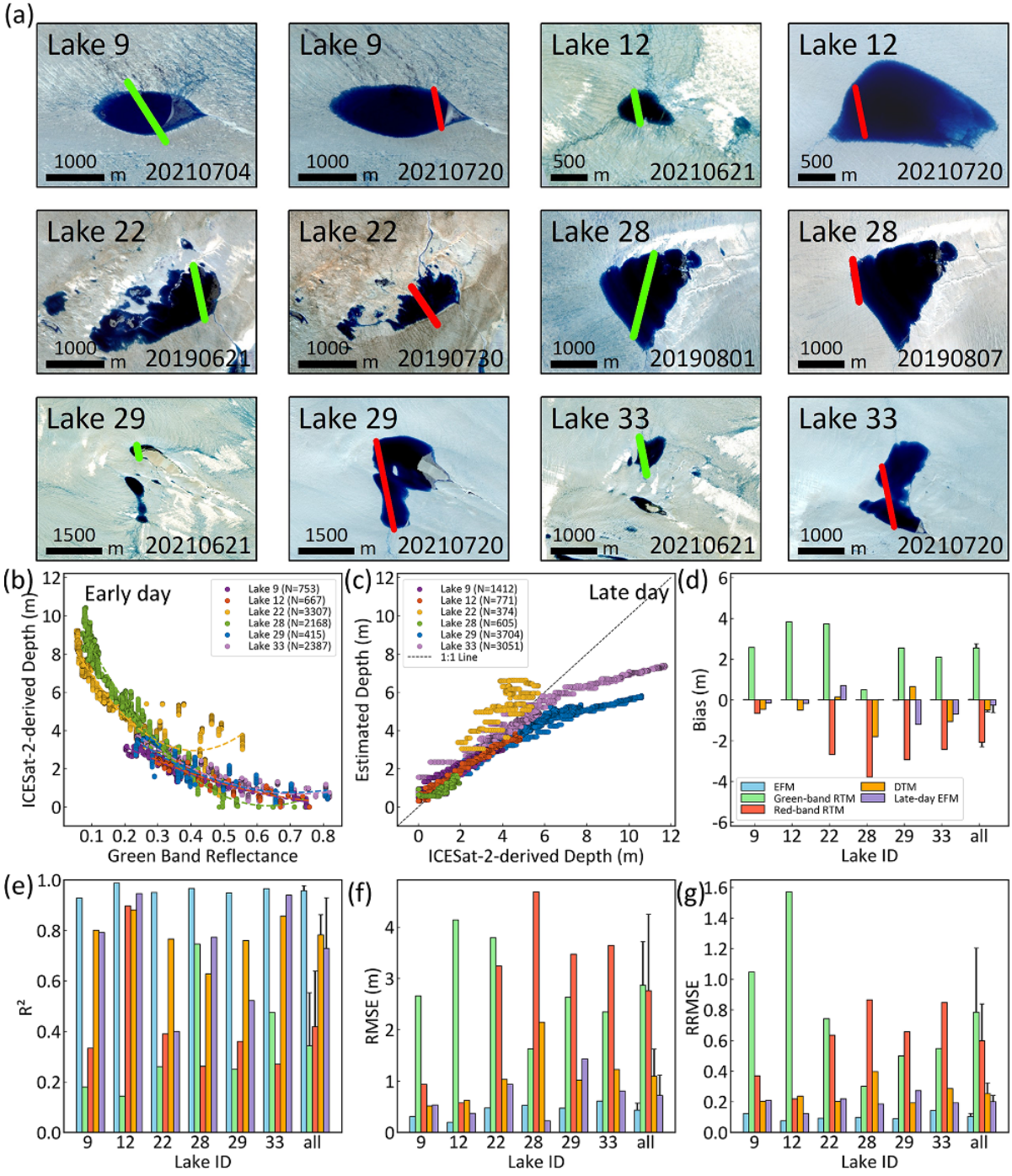

Figure 6. Temporal validation of the EFM using ICESat-2 tracks on different days. (a) Sentinel-2 images (R: NIR band, G: red band, B: green band) of six supraglacial lakes with two different ICESat-2 tracks on different days. The green and red lines represent the ICESat-2 tracks for early and late days, respectively. (b) Relationship between early-day green band reflectance and ICESat-2-derived depth for the six study lakes, and the dashed lines indicate the six fitted empirical formulas. (c) Comparison of late-day ICESat-2-derived depth and late-day lake depth estimated by applying the six early-day empirical formulas (i.e. Late-day EFM). (d) bias, (e) R^2, (f) RMSE, and (g) RRMSE (with the error bar showing the standard deviation) are calculated for the original EFM, RTM, DTM, and late-day EFM.

empirical formula performs significantly poorer than the empirical formula constructed for each lake (Fig. 5b), indicating that the EFM is challenging for spatial extrapolation. In previous studies, only one global empirical formula was used to estimate supraglacial lake depth over long periods (Box and Ski, 2007; Fitzpatrick and others, 2014) and large study areas (Fitzpatrick and others, 2014; Zhang and others, 2023). We suggest that this is problematic and recommend using EFM in small areas within the depth range of the training data used to construct the EFM.

The spatial extrapolation of the EFM is mainly limited by variable atmospheric conditions (Zhou and others, 2025), illumination angles (Wang and Zender, 2010), and snow/ice surfaces beneath and near lakes (Schröder and others, 2020). We suggest two approaches to mitigate these limitations: first, relative radiometric

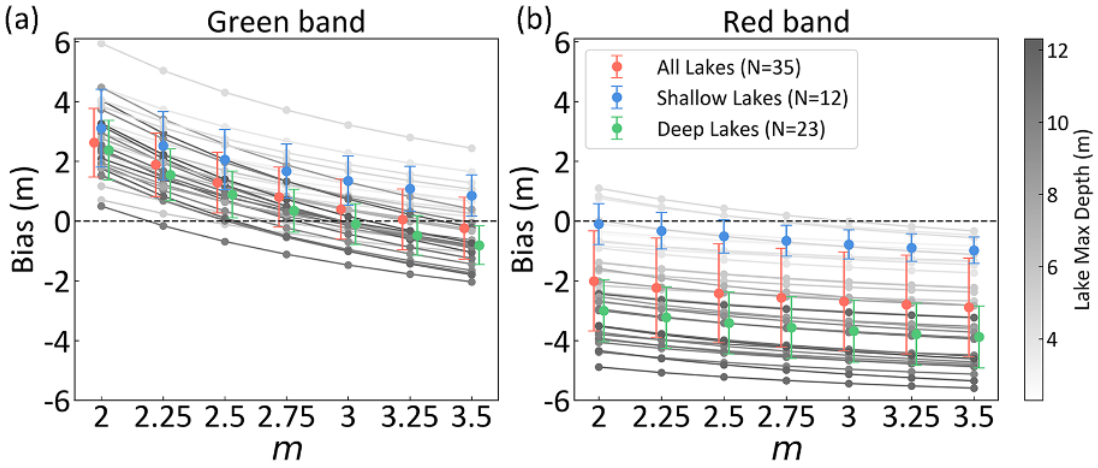

Figure 7. Sensitivity analysis of the *m* values in (a) green-band and (b) red-band radiative transfer methods (RTMs) based on 35 supraglacial lakes (max depth ~ 2.3–12.3 m, depth range ~ 10 m).

calibration (Carbonneau and others, 2006; Pahlevan and others, 2014) can be used to eliminate spectral inconsistence caused by different atmospheric conditions and illumination angles. Second, ice surface can be classified into different representative zones (e.g. bare ice zone, dry snow zone, and wet snow zone) based on satellite albedo products (Nolin and Payne, 2007; Shimada and others, 2016), and subsequently variable reflectance-depth empirical formulas can be built for different zones.

5.2. Applicability of the RTM

The performance of the green-band and red-band RTMs for estimating shallow and deep lake depths is demonstrated, respectively. The red band with longer wavelength attenuates more rapidly in water, resulting in higher accuracy for estimating shallow (max depth < 5 m) lake depth (owing to more distinguishable reflectance variations) but significantly underestimating deep lake depth (owing to stronger attenuation of deep water), whereas the green band with shorter wavelength performs better in estimating deep (max depth > 5 m) lake depth but significantly overestimating shallow lake depth (Figs. 2, 3; Table S2). These results are consistent with previous findings (Moussavi and others, 2016; Pope and others, 2016; Melling and others, 2024) but are more illustrative because lakes are explicitly classified as shallow and deep lakes and the corresponding quantitative over-/under- estimations are provided.

The variability of the spectral attenuation coefficient (g) limits the spatiotemporal extrapolation of the RTM. Melling and others (2024) recommended $m = 2.75$ (derived empirically as the average of the commonly used 2–3.5K_d range), whereas we recommend a different value, $g = 3K_d$ for green band RTM in deep lakes and $g = 2K_d$ for red band RTM in shallow lakes (Fig. 7). Spatiotemporal variation of g value (Kirk, 1989; Melling and others, 2024) may be induced by the non-negligible impurities (e.g. ice algae, snow algae, and light-absorbing impurities) at the bottom of the supraglacial lakes (Wang and others, 2018; Tedstone and others, 2020; Halbach and others, 2022), causing higher attenuation of the radiation. To handle the variability of g, an empirical reflectance threshold can be determined based on the red band to classify lake areas into shallow and deep areas. For example, based on our 35 study lakes, this threshold is ~0.08 (the average red band reflectance of points deeper than 5 m). As such, in shallow lake areas (red band reflectance > 0.08), the red band RTM with $g = 2K_d$ is recommended, while in deep lake areas (<0.08), the green band RTM with $g = 3K_d$ is recommended.

Like EFM, in previous studies, the green-band and red-band RTMs are widely used to estimate supraglacial lake depth over long time periods (Georgiou and others, 2009; Langley and others, 2016) and large study areas (Banwell and others, 2014; Williamson and others, 2017). We urge caution for using RTMs in this way because large spatiotemporal variations of GrIS supraglacial lake depths (McMillan and others, 2007; Sundal and others, 2009; Zhang and others, 2023) can greatly hinder the appropriate use of either the green-band or red-band RTM. Combining the RTM depth estimates from different bands may mitigate this problem, as suggested by Pope and others (2016), which used the arithmetic average of the red and the panchromatic band RTMs. However, we suggest that the improvement of band combinations is limited. If we combine green and red band RTMs, the overall RMSE values only slightly increase from 2.74–2.79 m to 1.86 m, whereas the improvement is not significant (Fig. S2). Alternatively, field-measured or ICESat-2-derived lake depth can be used to calibrate RTM's parameters, as per Moussavi and others (2016), but this will make RTM dependent on depth sample data as the EFM, thereby reducing the universality of the RTM. Instead, we suggest building a prior knowledge base of GrIS supraglacial lake depths based on the lake area, which positively correlates with lake depth (Sundal and others, 2009; Williamson and others, 2018a), or using the depression area/depth (Yang and others, 2019), which can directly reflect the possible maximum lake depth, and then selecting the green-band or red-band RTMs accordingly to calculate the depth of deep and shallow lakes, respectively.

5.3. Applicability of the DTM

In our comparison, the DTM yields the second-highest accuracy, indicating that it is a practical approach for estimating supraglacial lake depth, consistent with previous studies (Moussavi and others, 2016; Pope and others, 2016; Yang and others, 2019). However, we find the DTM systematically underestimates lake depth (Fig. 3; Table S2). For our 35 study lakes, the UR is

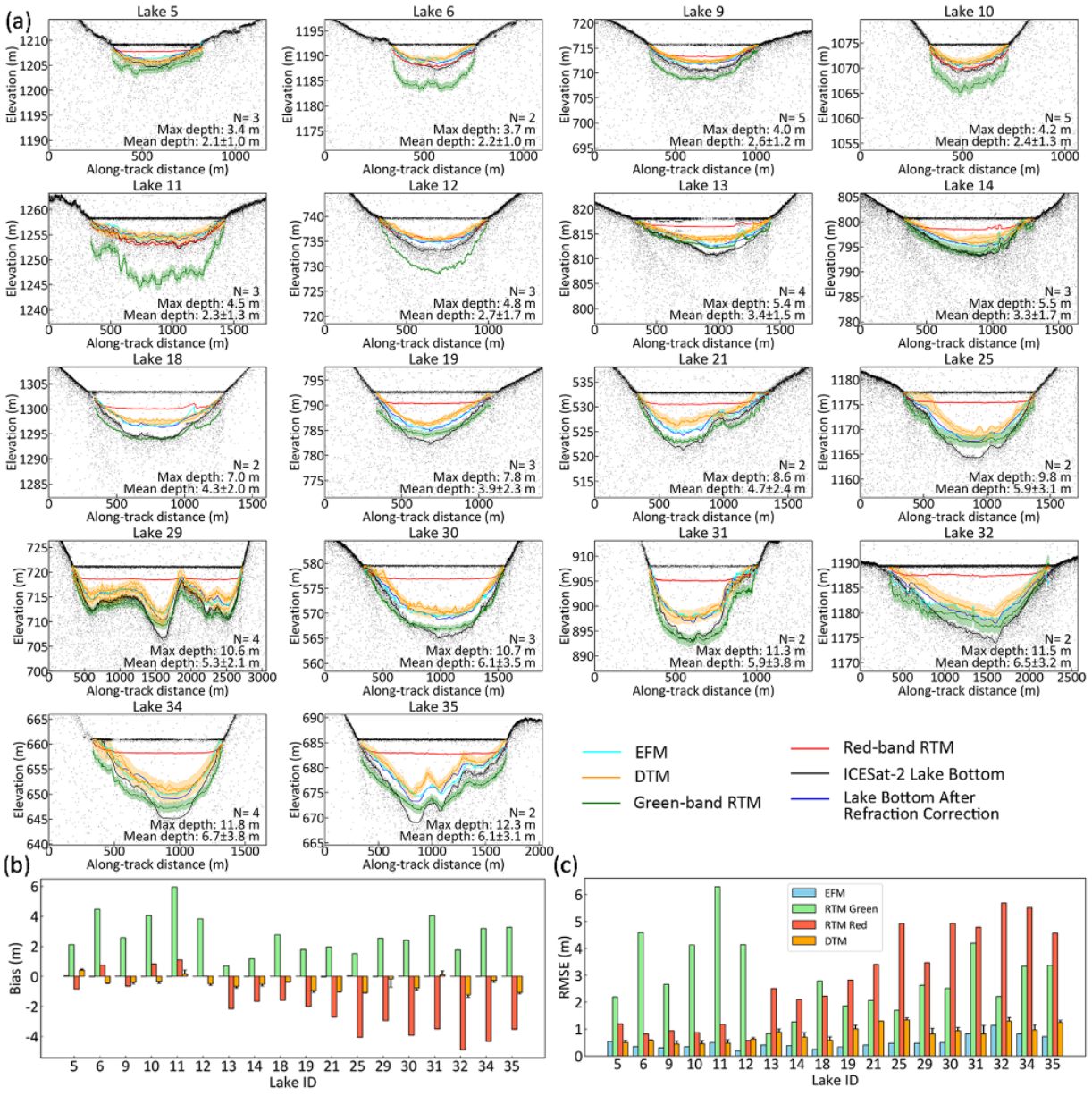

Figure 8. (a) Comparison of depth profiles estimated by depression topography method (DTM) using multi-period arcticdems, with the maximum uncertainty range (in orange) induced by the height differences of lake shoreline pixels, and (b) and (c) show the corresponding depth bias and RMSE for multi-period DTM (the error bars show the standard deviation) and other comparison methods.

14 ± 10%. This underestimation may be induced during the ArcticDEM product generation. The weak ice/snow texture in stereo satellite imagery may induce insufficient matching points and thereby considerable elevation bias, and the georeferenced matches between ArcticDEM and optical satellite imagery may also contain bias (Noh and Howat, 2015, 2017; Dai and others, 2024). These two factors may explain the height uncertainties (0.2–1.6 m) of the lake shoreline (Fig. 2). Moreover, the denoising process of ArcticDEM generation (Noh and Howat, 2017, 2019) may oversmooth the bottoms of topographic depressions, thereby systematically underestimating lake depths (Fig. 3). Furthermore, numerous supraglacial lakes do not exhibit dry-period 2 m ArcticDEM strips to date, although the future release of new ArcticDEM data may partially address this limitation.

Therefore, we currently need to rely on the simple UR for the better use of the DTM. We acknowledge that the possible transferability of this ratio over space and time is limited, so we recommend using it only for quantifying the DTM uncertainty (e.g. $1.14*D_{DTM}$) rather than rectifying the original DTM estimates. For example, Yang and others (2019) used DTM to estimate the depth and volume of two supraglacial lakes and discovered that the regional climate models overestimated the meltwater runoff on the GrIS by 106–123% (40–55% after early July) in the melt season, while the overestimation decreases to 80–95% (23–36% after early July) if applying our UR. In the future, DTM can be combined with the ICESat-2 data to create a dataset of dry depression topography on the GrIS and determine the corresponding URs for DTM-based depth estimation.

5.4. Impact of optical satellite resolutions on depth estimation

The optical satellite imagery resolution also influences the performance of EFM, RTM, and DTM. One 10 m resolution Sentinel-2 pixel covers ~14–20 ICESat-2 ATL03 points (~0.7 m along-track resolution), with the specific number depending on the interaction angle between Sentinel-2 pixels and ICESat-2 tracks. As such, the obtained reflectance-depth relationship may struggle in capturing small depth variations. Very high resolution (VHR) multispectral imagery (e.g. 2.44 m QuickBird, 1.64 m GeoEye-1, and 1.24–2.40 m WorldView-2/3/4) is potential for building more detailed and accurate reflectance-depth relationships. Moreover, for the DTM, VHR imagery may delineate more precise lake shorelines and thereby significantly reduce lake shoreline uncertainties. However, narrow swath (~10–20 km) VHR imagery often does not cover ocean regions, and thereby faces challenges to estimate deep ocean reflectance required for the RTM. In contrast, coarse resolution, wide swath imagery (e.g. 250 m MODIS, 500 m VIIRS, and 300 m Sentinel-3) may introduce large lake depth estimation uncertainty due to mixed pixel effects and imprecise shorelines.

6. Conclusion

In this study, we compare the performance of three remote sensing methods, namely the EFM, RTM, and DTM, to estimate supraglacial lake depth on the GrIS, with the ICESat-2-derived depth as validation data. Based on the comparison results, we recommend optimizing the use of these three methods. When field-measured depth or near-simultaneous ICESat-2 data are available, the green-band EFM is preferred, while we urge caution for the instability of empirical formulas and recommend using the EFM in small areas within the depth range of the training data used to construct the EFM. If no lake depth sample data are available, the DTM is recommended, yet an UR should be considered to quantify the DTM uncertainties. For the RTM, we recommend setting the spectral attenuation coefficient $g = 3K_d$ for the green band in deep lakes and $g = 2K_d$ for the red band in shallow lakes, and caution against the large-area use of the green-band or red-band RTMs. Viewing collectively, our method comparison may contribute to improving our understanding of GrIS surface meltwater storage and hydrological processes.

Supplementary material. The supplementary material for this article can be found at https://doi.org/10.1017/jog.2025.23

Acknowledgements. We acknowledge support from the National Key R&D Program (2022YFB3903601) and the National Natural Science Foundation of China (42271320). ArcticDEMs and geospatial support were provided by the Polar Geospatial Center under NSF-OPP awards (1043681, 1559691, 1542736, 1810976 and 2129685).

References

Albright A and Glennie C (2020) Nearshore bathymetry from fusion of Sentinel-2 and ICESat-2 observations. *IEEE Geoscience and Remote Sensing Letters* **18**(5), 900–904. doi:10.1109/LGRS.2020.2987778

Arndt PS and Fricker HA (2024) A framework for automated supraglacial lake detection and depth retrieval in ICESat-2 photon data across the Greenland and Antarctic ice sheets. *The Cryosphere* **18**(11), 5173–5206. doi:10.5194/tc-18-5173-2024

Arthur JF, Stokes CR, Jamieson SSR, Carr JR and Leeson AA (2020) Distribution and seasonal evolution of supraglacial lakes on Shackleton Ice Shelf, East Antarctica. *The Cryosphere* **14**(11), 4103–4120. doi:10.5194/tc-14-4103-2020

Banwell AF, Caballero M, Arnold NS, Glasser NF, Mac Cathles L and DR M (2014) Supraglacial lakes on the Larsen B ice shelf, Antarctica, and at Paakitsoq, West Greenland: A comparative study. *Annals of Glaciology* **55**(66), 1–8. doi:10.3189/2014AoG66A049

Bernardis M and 7 others (2023) Use of ICEsat-2 and Sentinel-2 open data for the derivation of bathymetry in shallow waters: Case studies in Sardinia and in the Venice Lagoon. *Remote Sensing* **15**(11), 2944. doi:10.3390/rs15112944

Box JE and Ski K (2007) Remote sounding of Greenland supraglacial melt lakes: Implications for subglacial hydraulics. *Journal of Glaciology* **53**(181), 257–265. doi:10.3189/172756507782202883

Brunt KM, Neumann TA and Smith BE (2019) Assessment of ICESat-2 ice sheet surface heights, based on comparisons over the interior of the Antarctic Ice Sheet. *Geophysical Research Letters* **46**(22), 13072–13078. doi:10.1029/2019GL084886

Buiteveld H, Hakvoort J and Donze M (1994) Optical properties of pure water. *Ocean Optics XII* **2258**, 174–183. doi:10.1117/12.190060

Carbonneau PE, Lane SN and Bergeron N (2006) Feature based image processing methods applied to bathymetric measurements from airborne remote sensing in fluvial environments. *Earth Surface Processes and Landforms* **31**(11), 1413–1423. doi:10.1002/esp.1341

Dai C and 9 others (2024) Applications of ArcticDEM for measuring volcanic dynamics, landslides, retrogressive thaw slumps, snowdrifts, and vegetation heights. *Science of Remote Sensing* **9**, 100130. doi: 10.1016/j.srs.2024.100130.

Das SB and 6 others (2008) Fracture propagation to the base of the Greenland Ice Sheet during supraglacial lake drainage. *Science* **320**(5877), 778–781. doi:10.1126/science.115336

Datta RT and Wouters B (2021) Supraglacial lake bathymetry automatically derived from ICESat-2 constraining lake depth estimates from multi-source satellite imagery. *The Cryosphere* **15**(11), 5115–5132. doi:10.5194/tc-15-5115-2021

Drusch M and 9 others (2012) Sentinel-2: ESA's optical high-resolution mission for GMES operational services. *Remote Sensing of Environment* **120**, 25–36. doi: 10.1016/j.rse.2011.11.026

Dunmire D, Banwell AF, Wever N, Lenaerts JTM and Datta RT (2021) Contrasting regional variability of buried meltwater extent over 2 years across the Greenland Ice Sheet. *The Cryosphere* **15**(6), 2983–3005. doi:10.5194/tc-15-2983-2021

Fair Z, Flanner M, Brunt KM, Fricker HA and Gardner A (2020) Using ICESat-2 and Operation IceBridge altimetry for supraglacial lake depth retrievals. *The Cryosphere* **14**(11), 4253–4263. doi:10.5194/tc-14-4253-2020

Fan Y, Ke C, Luo L, Shen X, Livingstone SJ and Lea JM (2025) Expansion of supraglacial lake area, volume and extent on the Greenland Ice Sheet from 1985 to 2023. *Journal of Glaciology* **71**, e4. doi:10.1017/jog.2024.87

Fitzpatrick AAW and 9 others (2014) A decade (2002–2012) of supraglacial lake volume estimates across Russell Glacier, West Greenland. *The Cryosphere* **8**(1), 107–121. doi:10.5194/tc-8-107-2014

Fricker HA and 12 others (2021) ICESat-2 Meltwater Depth Estimates: Application to Surface Melt on Amery Ice Shelf, East Antarctica. *Geophysical Research Letters* **48**(8), e2020GL090550. doi:10.1029/2020GL090550

Georgiou S, Shepherd A, McMillan M and Nienow P (2009) Seasonal evolution of supraglacial lake volume from ASTER imagery. *Annals of Glaciology* **50**(52), 95–100. doi:10.3189/172756409789624328

Halbach L and 14 others (2022) Pigment signatures of algal communities and their implications for glacier surface darkening. *Scientific Reports* **12**(1), 17643.10.1038/s41598-022-22271-4

Hsu HJ and 9 others (2021) A semi-empirical scheme for bathymetric mapping in shallow water by ICESat-2 and Sentinel-2: A case study in the South China Sea. *ISPRS Journal of Photogrammetry and Remote Sensing* **178**, 1–19. doi:10.1016/j.isprsjprs.2021.05.012

Ignéczi Á and 7 others (2016) Northeast sector of the Greenland Ice Sheet to undergo the greatest inland expansion of supraglacial lakes during the 21st century. *Geophysical Research Letters* **43**(18), 9729–9738. doi:10.1002/2016GL070338.

Ignéczi Á, Sole AJ, Livingstone SJ, Ng FS and Yang K (2018) Greenland Ice Sheet surface topography and drainage structure controlled by the transfer of basal variability. *Frontiers in Earth Science* **6**, 101. doi:10.3389/feart.2018.00101

Jasinski M and 10 others (2023) *ICESat-2 Algorithm Theoretical Basis Document(ATBD) for along Track Inland Surface Water Data, ATL13*, Version 6. *ICESat-2 Project*. doi: 10.5067/03JYGZ0758UL

Johansson AM and Brown IA (2013) Adaptive classification of supra-glacial lakes on the west Greenland Ice Sheet. *IEEE Journal of Selected Topics in Applied Earth Observations and Remote Sensing* **6**(4), 1998–2007. doi:10.1109/JSTARS.2012.2233722

Karlstrom L and Yang K (2016) Fluvial supraglacial landscape evolution on the Greenland Ice Sheet. *Geophysical Research Letters* **43**(6), 2683–2692. doi:10.1002/2016GL067697

Kirk JTO (1989) The upwelling light stream in natural waters. *Limnology and Oceanography* **34**(8), 1410–1425. doi:10.4319/lo.1989.34.8.1410

Langley ES, Leeson AA, Stokes CR and Jamieson SSR (2016) Seasonal evolution of supraglacial lakes on an East Antarctic outlet glacier. *Geophysical Research Letters* **43**(16), 8563–8571. doi:10.1002/2016GL069511

Legleiter CJ, Roberts DA and Lawrence RL (2009) Spectrally based remote sensing of river bathymetry. *Earth Surface Processes and Landforms* **34**(8), 1039–1059. doi:10.1002/esp.1787

Legleiter CJ, Tedesco M, Smith LC, Behar AE and Overstreet BT (2014) Mapping the bathymetry of supraglacial lakes and streams on the Greenland ice sheet using field measurements and high-resolution satellite images. *The Cryosphere* **8**(1), 215–228. doi:10.5194/tc-8-215-2014

Lutz K and 6 others (2024) Assessing supraglacial lake depth using ICESat-2, Sentinel-2, TanDEM-X, and in situ sonar measurements over Northeast and Southwest Greenland. *The Cryosphere* **18**(11), 5431–5449. doi:10.5194/tc-18-5431-2024

Lyzenga DR (1978) Passive remote sensing techniques for mapping water depth and bottom features. *Applied Optics* **17**(3), 379–383. doi:10.1364/AO.17.000379

Ma Y and 6 others (2020) Satellite-derived bathymetry using the ICESat-2 lidar and Sentinel-2 imagery datasets. *Remote Sensing of Environment* **250**, 112047. 10.1016/j.rse.2020.112047

Markus T and 24 others (2017) The Ice, Cloud, and land Elevation Satellite-2 (ICESat-2): Science requirements, concept, and implementation. *Remote Sensing of Environment* **190**, 260–273. doi: 10.1016/j.rse.2016.12.029.

McFeeters SK (1996) The use of the Normalized Difference Water Index (NDWI) in the delineation of open water features. *International Journal of Remote Sensing* **17**(7), 1425–1432. doi:10.1080/01431169608948714

McMillan M, Nienow P, Shepherd A, Benham T and Sole A (2007) Seasonal evolution of supra-glacial lakes on the Greenland Ice Sheet. *Earth and Planetary Science Letters* **262**(3), 484–492. doi:10.1016/j.epsl.2007.08.002

Melling L and 8 others (2024) Evaluation of satellite methods for estimating supraglacial lake depth in southwest Greenland. *The Cryosphere* **18**(2), 543–558. doi:10.5194/tc-18-543-2024

Morriss BF and 7 others (2013) A ten-year record of supraglacial lake evolution and rapid drainage in West Greenland using an automated processing algorithm for multispectral imagery. *The Cryosphere* **7**(6), 1869–1877. doi:10.5194/tc-7-1869-2013

Moussavi M, Pope A, Halberstadt ARW, Trusel LD, Cioffi L and Abdalati W (2020) Antarctic supraglacial lake detection using Landsat 8 and Sentinel-2 imagery: Towards continental generation of lake volumes. *Remote Sensing* **12**(1), 134. doi:10.3390/rs12010134

Moussavi MS and 6 others (2016) Derivation and validation of supraglacial lake volumes on the Greenland Ice Sheet from high-resolution satellite imagery. *Remote Sensing of Environment* **183**, 294–303. doi: 10.1016/j.rse.2016.05.024.

Neuenschwander A and Pitts K (2019) The ATL08 land and vegetation product for the ICESat-2 Mission. *Remote Sensing of Environment* **221**, 247–259. doi:10.1016/j.rse.2018.11.005

Nguyen QH and 7 others (2021) Influence of data splitting on performance of machine learning models in prediction of shear strength of soil. *Mathematical Problems in Engineering* **2021**(1), 4832864. doi:10.1155/2021/4832864

Noh MJ and Howat IM (2015) Automated stereo-photogrammetric DEM generation at high latitudes: Surface Extraction with TIN-based Search-space Minimization (SETSM) validation and demonstration over glaciated regions. *GIScience & Remote Sensing* **52**(2), 198–217. doi:10.1080/15481603.2015.1008621

Noh MJ and Howat IM (2017) The surface extraction from TIN based search-space minimization (SETSM) algorithm. *ISPRS Journal of Photogrammetry and Remote Sensing* **129**, 55–76. doi:10.1016/j.isprsjprs.2017.04.019

Noh MJ and Howat IM (2019) Applications of high-resolution, cross-track, pushbroom satellite images with the SETSM algorithm. *IEEE Journal of Selected Topics in Applied Earth Observations and Remote Sensing* **12**(10), 3885–3899. doi:10.1109/JSTARS.2019.2938146

Nolin AW and Payne MC (2007) Classification of glacier zones in western Greenland using albedo and surface roughness from the Multi-angle Imaging SpectroRadiometer (MISR). *Remote Sensing of Environment* **107**(1–2), 264–275. doi:10.1016/j.rse.2006.11.004

Pahlevan N, Lee Z, Wei J, Schaaf CB, Schott JR and Berk A (2014) On-orbit radiometric characterization of OLI (Landsat-8) for applications in aquatic remote sensing. *Remote Sensing of Environment* **154**, 272–284. doi:10.1016/j.rse.2014.08.001

Parrish CE, Magruder LA, Neuenschwander AL, Forfinski-Sarkozi N, Alonzo M and Jasinski M (2019) Validation of ICESat-2 ATLAS bathymetry and analysis of ATLAS's bathymetric mapping performance. *Remote Sensing* **11**(14), 1634. doi:10.3390/rs11141634

Philpot WD (1989) Bathymetric mapping with passive multispectral imagery. *Applied Optics* **28**(8), 1569–1578. doi:10.1364/AO.28.001569

Pope A and 6 others (2016) Estimating supraglacial lake depth in West Greenland using Landsat 8 and comparison with other multispectral methods. *The Cryosphere* **10**1, 15–27. doi:10.5194/tc-10-15-2016.

Pope RM and Fry ES (1997) Absorption spectrum (380–700 nm) of pure water. II. Integrating cavity measurements. *Applied Optics* **36**(33), 8710–8723. doi:10.1364/AO.36.008710

Porter C and 18 others (2022) ArcticDEM - strips, version 4.1. Harvard Dataverse doi:10.7910/DVN/C98DVS

Ranndal H, Sigaard Christiansen P, Kliving P, Baltazar Andersen O and Nielsen K (2021) Evaluation of a statistical approach for extracting shallow water bathymetry signals from ICESat-2 ATL03 photon data. *Remote Sensing* **13**(17), 3548. doi:10.3390/rs13173548

Rowley N, Rancher W and Karmosky C (2024) Comparison of Multiple Methods for Supraglacial Melt-Lake Volume Estimation in Western Greenland During the 2021 Summer Melt Season. *Glacies* **1**(2), 92–110. doi:10.3390/glacies1020007

Schröder L, Neckel N, Zindler R and Humbert A (2020) Perennial supraglacial lakes in Northeast Greenland observed by polarimetric SAR. *Remote Sensing* **12**(17), 2798. doi:10.3390/rs12172798

Shimada R, Takeuchi N and Aoki T (2016) Inter-annual and geographical variations in the extent of bare ice and dark ice on the Greenland ice sheet derived from MODIS satellite images. *Frontiers in Earth Science* **4**, 43. doi:10.3389/feart.2016.00043

Smith B and 9 others (2019) Land ice height-retrieval algorithm for NASA's ICESat-2 photon-counting laser altimeter. *Remote Sensing of Environment* **233**, 111352. doi: 10.1016/j.rse.2019.111352.

Sneed WA and Hamilton GS (2007) Evolution of melt pond volume on the surface of the Greenland Ice Sheet. *Geophysical Research Letters* **34**(3). doi:10.1029/2006gl028697

Sneed WA and Hamilton GS (2011) Validation of a method for determining the depth of glacial melt ponds using satellite imagery. *Annals of Glaciology* **52**(59), 15–22. doi:10.3189/172756411799096240

Sundal AV, Shepherd A, Nienow P, Hanna E, Palmer S and Huybrechts P (2009) Evolution of supra-glacial lakes across the Greenland Ice Sheet. *Remote Sensing of Environment* **113**(10), 2164–2171. doi:10.1016/j.rse.2009.05.018

Tedesco M and Steiner N (2011) In-situ multispectral and bathymetric measurements over a supraglacial lake in western Greenland using a remotely controlled watercraft. *The Cryosphere* **5**(2), 445–452. doi:10.5194/tc-5-445-2011

Tedstone AJ and 7 others (2020) Algal growth and weathering crust state drive variability in western Greenland Ice Sheet ice albedo. *The Cryosphere* **14**(2), 521–538. doi:10.5194/tc-14-521-2020

Tuckett PA and 6 others (2019) Rapid accelerations of Antarctic Peninsula outlet glaciers driven by surface melt. *Nature Communications* **10**(1), 4311. doi:10.1038/s41467-019-12039-2

Wang S, Tedesco M, Xu M and Alexander PM (2018) Mapping ice algal blooms in southwest Greenland from space. *Geophysical Research Letters* **45**(21), 11,779–11,788. doi:10.1029/2018GL080455

Wang X and Zender CS (2010) MODIS snow albedo bias at high solar zenith angles relative to theory and to in situ observations in Greenland. *Remote Sensing of Environment* **114**(3), 563–575. doi:10.1016/j.rse.2009.10.014

Williamson AG, Arnold NS, Banwell AF and Willis IC (2017) A Fully Automated Supraglacial lake area and volume Tacking ("FAST") algorithm: Development and application using MODIS imagery of West Greenland. *Remote Sensing of Environment* **196**, 113–133. doi:10.1016/j.rse.2017.04.032

Williamson AG, Banwell AF, Willis IC and Arnold NS (2018a) Dual-satellite (Sentinel-2 and Landsat-8) remote sensing of supraglacial lakes in Greenland. *The Cryosphere* **12**(9), 3045–3065. doi:10.5194/tc-12-3045-2018

Williamson AG, Willis IC, Arnold NS and Banwell AF (2018b) Controls on rapid supraglacial lake drainage in West Greenland: An Exploratory Data Analysis approach. *Journal of Glaciology* **64**(244), 208–226. doi:10.1017/jog.2018.8

Xiao W, Hui F, Cheng X and Liang Q (2023) An automated algorithm to retrieve the location and depth of supraglacial lakes from ICESat-2 ATL03 data. *Remote Sensing of Environment* **298**, 113730. doi:10.1016/j.rse.2023.113730

Xu N, Ma X, Ma Y, Zhao P, Yang J and Wang XH (2021) Deriving highly accurate shallow water bathymetry from Sentinel-2 and ICESat-2 datasets by a multitemporal stacking method. *IEEE Journal of Selected Topics in Applied Earth Observations and Remote Sensing* **14**, 6677–6685. doi:10.1109/JSTARS.2021.3090792

Yang K, Smith LC, Fettweis X, Gleason CJ, Lu Y and Li M (2019) Surface meltwater runoff on the Greenland ice sheet estimated from remotely sensed supraglacial lake infilling rate. *Remote Sensing of Environment* **234**, 111459. doi:10.1016/j.rse.2019.111459

Zhang W and 7 others (2023) Pan-Greenland mapping of supraglacial rivers, lakes, and water-filled crevasses in a cool summer (2018) and a warm summer (2019). *Remote Sensing of Environment* **297**, 113781. doi: 10.1016/j.rse.2023.113781.

Zhou Q, Liang Q, Xiao W, Li T, Zheng L and Cheng X (2025) Supraglacial Lake Depth Retrieval from ICESat-2 and Multispectral Imagery Datasets. *Journal of Remote Sensing* **5**, 0416. doi:10.34133/remotesensing.0416

Zhu D, Zhou C, Zhu Y and Peng B (2022) Evolution of supraglacial lakes on Sermeq Avannarleq glacier, Greenland using Google Earth Engine. *Journal of Hydrology: Regional Studies* **44**, 101246. doi:10.1016/j.ejrh.2022.101246